Coordinate-Transformed Dynamic Mode Decomposition for Short-Term Rainfall Forecasting

Shitao Zheng, Takashi Miyamoto, *Member, IEEE*, Shingo Shimizu, Ryohei Kato, and Koyuru Iwanami

***Abstract*— Lagrangian persistence method in nowcasting is a highly effective method for short-term weather forecasting. However, its performance is not as robust in long-term forecasting or situations of rapid weather changes due to the difficulty in analyzing the intensity variation of meteorological physical quantities. To address this shortcoming, in this study, we incorporated dynamic mode decomposition (DMD) into the Lagrangian persistence method. Specifically, we proposed a coordinate-transformed DMD (CT-DMD) model by integrating an optical flow model with a DMD model, providing an effective method for analyzing the intensity variation of meteorological physical quantities in the Lagrangian persistence method. The integration of the optical flow model and the DMD model involves the transformation of data between Eulerian and Lagrangian coordinate systems. The CT-DMD model was evaluated using radar-observed rainfall data from the Kanto region of Japan, with the Rainymotion model used as a benchmark. When the lead time was 5 min, 22.22% of the subsets in the experimental dataset showed that the CT-DMD model had a higher forecast accuracy compared to the Rainymotion model. When the lead time was 25 min, 88.89% of the subsets in the experimental dataset showed that the CT-DMD model had a higher forecast accuracy compared to the Rainymotion model. The accuracy advantage of the CT-DMD model became apparent after a lead time of 15 min and became increasingly significant as the lead time increased. The results demonstrated the validity of the CT-DMD model.**

***Index Terms*— Data-driven model, dynamic mode decomposition (DMD), nowcasting, optical flow, radar-observed data, short-term rainfall forecasting.**

I. Introduction

In THE field of meteorological forecasting, forecasting models can be classified into two categories, numerical weather prediction (NWP) and extrapolation-based nowcasting (hereafter referred to as nowcasting), depending on the length of lead time [1].

When the lead time is longer than 2 h, the NWP model is an appropriate choice for forecasting because it can sufficiently simulate the coupled physical equations of weather to forecast weather conditions. However, when the lead time is shorter than 2 h, the forecasting accuracy of the NWP model is compromised because of both insufficient spin-up time and difficulties in applying non-Gaussian data assimilation [2], [3], [4].

When the lead time is shorter than 2 h, the nowcasting model is more effective than the NWP model. Since the 1960s, with the improvement in the quality of radar and satellite observational data, particularly regarding precipitation or proxies, the predictive method of very short-range, local forecasting by extrapolation has gradually shown promising prospects [2]. Browning [5] clarified the relative advantages of nowcasting model and NWP model, highlighting that the former exhibits higher accuracy within short-term forecasting. In the initial stage, the nowcasting model typically focuses on analyzing and extrapolating the trends of individual variables, such as rainfall distribution [6]. However, with the development of technology and algorithms, numerous nowcasting models are employing a range of radar products, algorithms, and blending techniques with the aim of providing forecasts up to 1–3 h [7], for example, ANC [8], MAPLE [9], RADVOR [10], STEPS [11], STEPS-BE [12], and SWIRLS [13], [14].

When data are limited to radar images alone, in situations where there is insufficient weather condition information, a commonly used forecasting method in nowcasting models is to extrapolate the field of meteorological physical quantities based on the assumed constant intensity of these quantities. This method is known as the Lagrangian persistence [9], for example, Rainymotion model [7]. It can be observed that the Lagrangian persistence method is suitable for relatively stable weather conditions in the short term. However, for long-term forecasting or situations with rapid changes in weather conditions in the short term, the forecasting accuracy of the Lagrangian persistence method is severely reduced because of the difficulty in analyzing the intensity variation of meteorological physical quantities. To overcome this difficulty, one scheme is to introduce a source-sink term to the Lagrangian persistence method, which enables the analysis and forecasting of the intensity variations of meteorological

Manuscript received 27 November 2023; revised 11 March 2024; accepted 23 March 2024. Date of publication 29 March 2024; date of current version 8 April 2024. This work was supported by the Japan Society for the Promotion of Science (JSPS) Grants-in-Aid for Scientific Research (KAKENHI) under Grant JP23H01656. *(Corresponding author: Takashi Miyamoto.)*

Shitao Zheng is with the School of Engineering, Institute of Engineering Innovation, The University of Tokyo, Bunkyo, Tokyo 113-0033, Japan (e-mail: aysz3028@g.ecc.u-tokyo.ac.jp).

Takashi Miyamoto is with the Department of Civil and Environmental Engineering, University of Yamanashi, Kofu, Yamanashi 400-8511, Japan, and also with German Research Center for Artificial Intelligence, 67663 Kaiserslautern, Germany (e-mail: tmiyamoto@yamanashi.ac.jp).

Shingo Shimizu, Ryohei Kato, and Koyuru Iwanami are with the National Research Institute for Earth Science and Disaster Resilience, Tsukuba, Ibaraki 305-0006, Japan (e-mail: shimizus@bosai.go.jp; rkato@bosai.go.jp; iwanami@bosai.go.jp).

Digital Object Identifier 10.1109/TGRS.2024.3383058

physical quantities [9]. In this article, we utilize the dynamic mode decomposition (DMD) model to implement the function of the source-sink term in the Lagrangian persistence method, providing a novel and effective model for rainfall forecasting using only radar images.

Recently, with the increase in computing power and the rapid development of big data, scientists have begun to introduce novel data-driven models to overcome the inherent limitations of traditional weather forecasting models.

As an important category of data-driven models, deep-learning models have made significant contributions to meteorological forecasting in recent years [15], [16], [17], [18], [19]. Byun et al. [20] introduced a new research direction that utilizes cloud image data as input, employing a deep-learning model for analysis and prediction of rainfall amount. Wang et al. [21] proposed a deep-learning model for heavy rainfall nowcasting based on task-segmented architecture. Unlike traditional forecasting methods, deep-learning models can automatically adjust the parameters within a model using a loss function to calculate the gap between the forecast output and target data. This imparts the ability to explore the hidden nonlinear connections between the input and target data. However, despite their high performance in exploring connections between the input and target data, in the field of meteorological forecasting, the deep-learning models still have limitations such as the problem of spatial smoothing [22].

However, another category of data-driven models makes predictions by discovering hidden patterns of development in the data. Relying on sparsity-promoting techniques, Brunton et al. [23] and Rudy et al. [24] proposed a new sparse regression method to discover the governing partial differential equations underlying dynamical systems through data measurements. Raissi et al. [25], [26] proposed a method based on Gaussian processes to infer the parameters of governing equations expressed by parametric linear operators from scarce and possibly noisy observations.

Considering this background, in this study, we aim to address the difficulty of analyzing the intensity variation of meteorological physical quantities in the Lagrangian persistence method by incorporating a data-driven model, DMD model, into the Lagrangian persistence method. Based on the principles of the rainfall process, we propose a data-driven model for forecasting future rainfall by analyzing patterns within the rainfall process. The proposed model was validated using radar-observed rainfall data from the Kanto region of Japan.

II. Proposed Method: Coordinate-Transformed Dynamic Mode Decomposition

A. Overview of the Proposed Method

The governing equations that describe the processes of rainfall phenomena can be divided into two categories: those related to rainfall intensity variation, which involves cloud microphysics [27], [28], and those related to atmospheric motion, which involves hydrodynamics [29]. Based on this characteristic, for forecasting rainfall, we propose a data-driven model that combines the DMD and optical flow models. The DMD model was employed to analyze rainfall intensity variations, and the optical flow model was employed to analyze atmospheric motion. This hybrid model effectively combines the strengths of the DMD model in analyzing the intensity changes in physical quantities with the strengths of the optical flow model in capturing the velocity field in physical quantities. In the construction of the proposed model, the combination of the optical flow model and the DMD model involves the transformation of data between the Eulerian and Lagrangian coordinate systems. Fig. 1 shows a conceptual diagram of the proposed model.

B. Optical Flow

Horn and Schunck [30] introduced the term optical flow, which is defined as the distribution of apparent velocities of the movement of brightness patterns in an image. When there is relative motion between the observer and the object, an optical flow is generated [31], [32]. Thus, by analyzing the optical flow, spatial information about an object can be obtained [33].

Today, with the development of computer technology, optical flow can be used as an algorithm to analyze velocity fields from radar-observed data. Optical flow has been extensively used in the field of rainfall nowcasting [14], [34], [35]. Ayzel et al. [7] compared optical-flow-based precipitation forecasting models with the state-of-the-art operational software RADVOR (radar real-time forecasting) model, demonstrating that the former has comparable or higher forecasting accuracy than the latter. Moreover, they organized these optical-flow-based precipitation forecasting models into a Python library called "Rainymotion."

Therefore, in this study, we use the "Dense model" from the "Rainymotion" Python library as a benchmark for evaluating our proposed model [coordinate-transformed DMD (CT-DMD)]. Hereafter, we refer to the "Dense model" as "Rainymotion."

The Rainymotion model can be summarized in the following three steps.

1) First, the DIS optical flow model [36] is used to calculate the velocity field $\mathbf{V}_{m-1}$ based on data at time t_{m-1} and t_m.
2) To extrapolate the data at time point t_m, a backward constant-vector scheme is used [34].
3) The extrapolated data are interpolated using the inverse distance weighting method.

In rainfall forecasting, the objective of the Rainymotion model is to calculate the velocity of each rainfall cell based on the recent state of rainfall and then extrapolate the rainfall cells along the time axis. Therefore, this forecasting does not allow the analysis of the changes in the intensity of each cell. These characteristics are evident in the forecast results of the Rainymotion model in Fig. 15.

C. Dynamic Mode Decomposition

Schmid [37] proposed an algorithm called the DMD to identify spatiotemporally coherent structures from high-dimensional data [38]. This algorithm can analyze a series of modes from time-series data, with each mode corresponding to a coefficient that encapsulates the information of the oscillation frequency and growth/decline amplitude of the mode. From these modes and coefficients, the characteristics of the

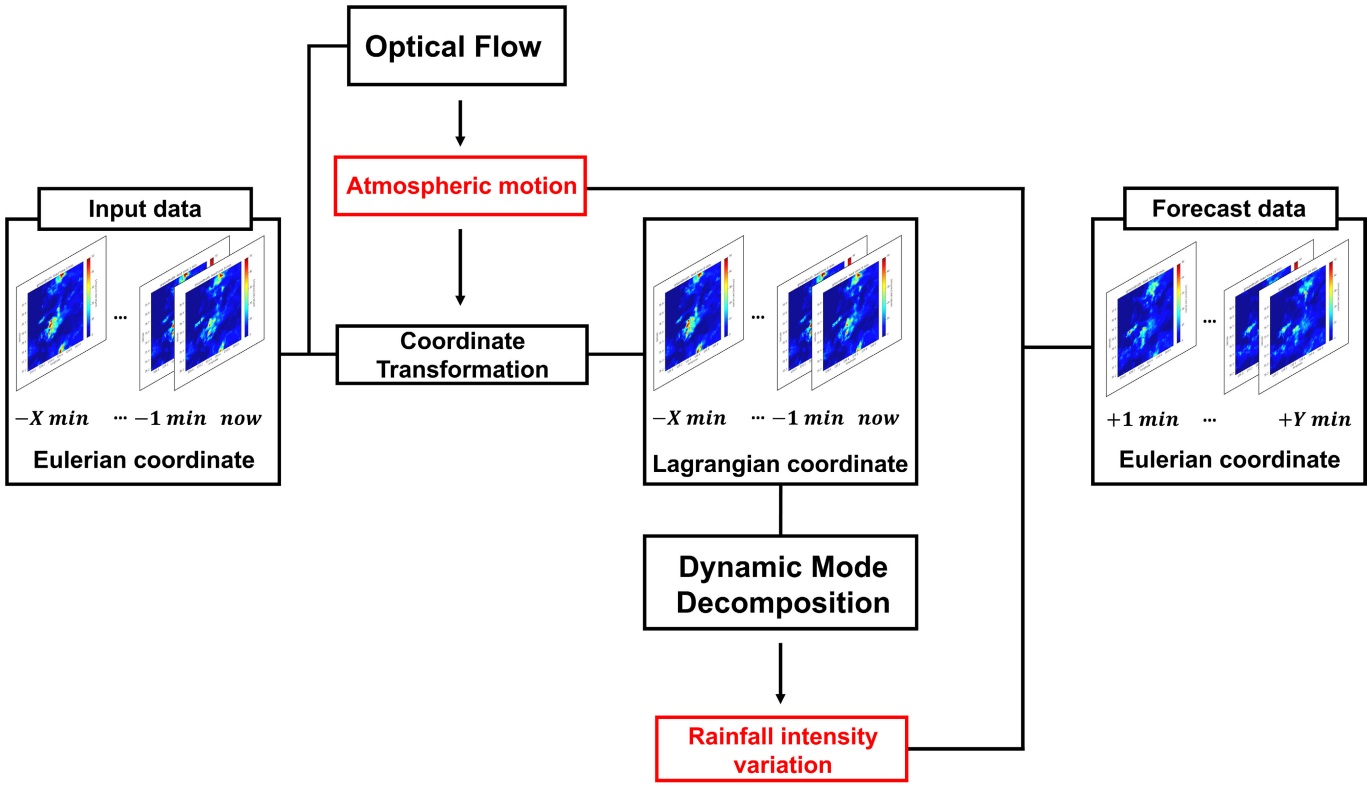

Fig. 1. Conceptual diagram of the proposed model.

time-series data can be determined, enabling the forecasting of time-series data. In the field of data analysis, DMD is widely used [39], [40]; moreover, DMD can potentially be applied to the study of coordinated control systems [41].

The DMD algorithm is briefly described as follows.

There are various algorithms for DMD. In this study, we use the DMD algorithm developed by Tu et al. [42]. We utilized the "PyDMD" library [43] to implement the DMD algorithm.

First, we denote a set of time-series data as $\{\mathbf{x}(t_0), \mathbf{x}(t_1), \mathbf{x}(t_2), \ldots, \mathbf{x}(t_m), \mathbf{x}(t_{m+1})\}$, where each $\mathbf{x}$ is a column vector. Next, we construct two matrices with the time-series data

$$\mathbf{X} = \begin{bmatrix} | & | & | & | & | \\ \mathbf{x}(t_0) & \mathbf{x}(t_1) & \mathbf{x}(t_2) & \cdots & \mathbf{x}(t_m) \\ | & | & | & | & | \end{bmatrix}$$

$$\mathbf{Y} = \begin{bmatrix} | & | & | & | & | \\ \mathbf{x}(t_1) & \mathbf{x}(t_2) & \mathbf{x}(t_3) & \cdots & \mathbf{x}(t_{m+1}) \\ | & | & | & | & | \end{bmatrix}.$$

We observe that $\mathbf{Y}$ is the lagged sequence of $\mathbf{X}$. The objective of the DMD algorithm is to determine the dominant spectral decomposition of optimal linear operator $\mathbf{A}$ that best fits the given datasets $\mathbf{X}$ and $\mathbf{Y}$ [38]

$$\mathbf{Y} \approx \mathbf{A}\mathbf{X}$$
$$\mathbf{A} = \arg\min_{\mathbf{A}} \|\mathbf{Y} - \mathbf{A}\mathbf{X}\|_F = \mathbf{Y}\mathbf{X}^{\dagger}$$
$$A = \Phi \Lambda \Phi^{\dagger}$$

where variables are defined as follows.

1) $\|\cdot\|_F$: Frobenius norm.
2) $\dagger$: Pseudoinverse.
3) Φ: A matrix consisting of the eigenvectors of $\mathbf{A}$, where each eigenvector ϕ is referred to as a DMD mode.
4) Λ: A diagonal matrix consisting of the eigenvalues of $\mathbf{A}$, where each eigenvalue λ is referred to as a DMD eigenvalue.

When the sizes of $\mathbf{X}$ and $\mathbf{Y}$ are small, DMD eigenvalues Λ and DMD modes Φ of $\mathbf{A}$ can be calculated by performing the spectral decomposition of $\mathbf{A}$.

However, when the sizes of the $\mathbf{X}$ and $\mathbf{Y}$ matrices are large, it is unwieldy to perform the direct spectral decomposition of matrix $\mathbf{A}$, in which case the exact DMD algorithm can help us extract only the important eigenvalues Λ and eigenvectors Φ in $\mathbf{A}$.

Then, future time-series data can be forecast using Φ and Λ

$$\mathbf{x}(t_k) = \Phi \Lambda^k \Phi^{\dagger} \mathbf{x}(t_0) = \sum_{i=1}^{M} \phi_i \lambda_i^k \phi_i^{\dagger} \mathbf{x}(t_0).$$

However, the DMD algorithm has limitations because it does not correctly decompose the patterns of convective phenomena, which hinders its application in rainfall forecasting [44]. These characteristics are evident in the forecast results of the DMD algorithm shown in Fig. 15. Although the DMD algorithm correctly forecasts the declining rainfall trend, it does not accurately forecast atmospheric motion.

D. CT-DMD: Concept of Model Construction

As discussed above, it can be observed that both the Rainymotion model and the DMD model have inherent limitations. The Rainymotion model can analyze and forecast atmospheric motion but is unable to effectively analyze and forecast

rainfall intensity variation. Conversely, the DMD model can analyze and forecast rainfall intensity variation but is unable to effectively analyze and forecast atmospheric motion.

In this study, we aim to construct an integrated model using the optical flow and DMD models for analyzing and forecasting rainfall intensity variation and atmospheric motion simultaneously.

The main idea of this integration involves the transformation of data between the Eulerian and Lagrangian coordinate systems; therefore, we named this integrated CT-DMD model.

For analyzing rainfall processes, the Eulerian and Lagrangian coordinate systems have their own advantages.

The Eulerian coordinate system is a system of fixed coordinate axes that, in the field of fluid dynamics, presents the spatial distribution of fluid at each moment in time [45]. Through the Eulerian coordinate system, we are able to observe the relationship between the position of fluid over time.

On the other hand, the Lagrangian coordinate system is a coordinate system that emphasizes the fluid quantities' own intrinsic changes. Unlike the Eulerian coordinate system, the Lagrangian coordinate system is not fixed at a particular location in space but is attached to the fluid quantities and changes continuously with the movement of the fluid quantities. In the Lagrangian coordinate system, we can define the flow quantities as functions of time and a chosen element of fluid matter [45]. Through this function, we are able to observe the dynamics of the selected fluid element itself over time.

For the rainfall process, it can be divided into two components: rainfall intensity variation and atmospheric motion. Rainfall intensity variation, related to cloud microphysics, is suitable for analysis under the Lagrangian coordinate system, which emphasizes the observation of the intrinsic changes in fluid quantities. Atmospheric motion, related to fluid dynamics, is suitable for analysis under the Eulerian coordinate system, which emphasizes the observation of the spatial distribution of fluid.

By dividing the rainfall process into two components, rainfall intensity variation and atmospheric motion, and analyzing them separately in the Lagrangian and Eulerian coordinate systems, we believe that this method of constructing the model is more mathematically sound and capable of accurately analyzing rainfall.

E. CT-DMD: Algorithmic Principle

The algorithmic principle of the CT-DMD model is as follows.

Initially, define a set of 2-D time-series data $\{\mathbf{x}_E(t_0), \mathbf{x}_E(t_1), \mathbf{x}_E(t_2), \ldots, \mathbf{x}_E(t_m)\}$ in the Eulerian coordinate system. In this study, each $\mathbf{x}_E$ represents a 2-D rainfall distribution with fixed latitude and longitude.

1) First, the optical flow model is used to calculate the velocity field $\mathbf{V}_k$ between each pair of adjacent time-series data $\{\mathbf{x}_E(t_k), \mathbf{x}_E(t_{k+1})\}$

$$\mathbf{V}_k = \text{Optical Flow}(\mathbf{x}_E(t_k), \mathbf{x}_E(t_{k+1})) \times (k = 0, \ldots, m-1).$$

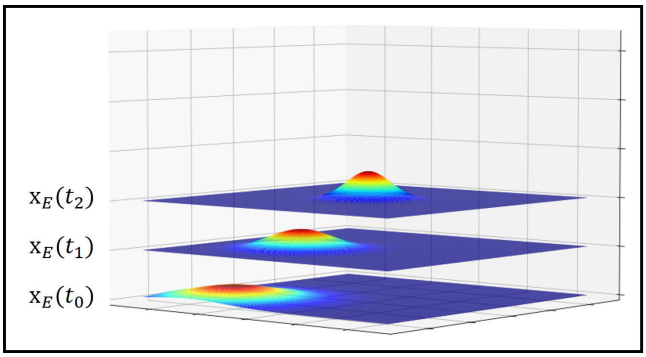

Fig. 2. Step 1 of illustrative example, define a set of 2-D time-series data and use the optical flow model to calculate velocity fields.

2) By using velocity fields $\{\mathbf{V}_0, \mathbf{V}_1, \mathbf{V}_2, \ldots, \mathbf{V}_{m-1}\}$, time-series data in the Eulerian coordinate system $\{\mathbf{x}_E(t_0), \mathbf{x}_E(t_1), \mathbf{x}_E(t_2), \ldots, \mathbf{x}_E(t_m)\}$ can be converted to those in the Lagrangian coordinate system $\{\mathbf{x}_L(t_0), \mathbf{x}_L(t_1), \mathbf{x}_L(t_2), \ldots, \mathbf{x}_L(t_m)\}$

$$\mathbf{x}_L(t_k) = \text{Convert}_{EL}(\mathbf{x}_E(t_k), \{\mathbf{V}_k, \mathbf{V}_{k+1}, \ldots, \mathbf{V}_{m-1}\}) \times (k = 0, \ldots, m-1)$$

where Convert_{EL} is a method for converting time-series data from the Eulerian to Lagrangian coordinate system and m is the reference time point for converting the data from the Eulerian $\mathbf{x}_E$ to Lagrangian coordinate system $\mathbf{x}_L$. Also, $\mathbf{x}_E(t_m)$ is equal to $\mathbf{x}_L(t_m)$, and no conversion is needed.

3) Time-series data in the Lagrangian coordinate system $\{\mathbf{x}_L(t_0), \mathbf{x}_L(t_1), \mathbf{x}_L(t_2), \ldots, \mathbf{x}_L(t_m)\}$ are analyzed using the DMD model. Next, the analyzed DMD modes Φ and DMD eigenvalues Λ are used to forecast time-series data $\{\mathbf{x}_L(t_{m+1}), \mathbf{x}_L(t_{m+2}), \mathbf{x}_L(t_{m+3}), \ldots, \mathbf{x}_L(t_{m+n})\}$

$$\mathbf{x}_L(t_k) = \Phi\Lambda^k\Phi^\dagger\mathbf{x}_L(t_0) = \sum_{i=1}^{M}\phi_i\lambda_i^k\phi_i^\dagger\mathbf{x}_L(t_0) \times (k = m+1, \ldots, m+n).$$

4) The velocity field after reference time point m is assumed to remain consistent with $\mathbf{V}_{m-1}$, and by using velocity field $\{\mathbf{V}_{m-1}\}$ for extrapolation, time-series data in the Lagrangian coordinate system $\{\mathbf{x}_L(t_{m+1}), \mathbf{x}_L(t_{m+2}), \mathbf{x}_L(t_{m+3}), \ldots, \mathbf{x}_L(t_{m+n})\}$ can be converted back to those in the Eulerian coordinate system $\{\mathbf{x}_E(t_{m+1}), \mathbf{x}_E(t_{m+2}), \mathbf{x}_E(t_{m+3}), \ldots, \mathbf{x}_E(t_{m+n})\}$

$$\mathbf{x}_E(t_k) = \text{Convert}_{LE}(\mathbf{x}_L(t_k), \{V_{m-1}, \ldots, V_{m-1}\}) \times (k = m+1, \ldots, m+n).$$

where the Convert_{LE} function is a method for converting time-series data from the Lagrangian to Eulerian coordinate system, and the number of extrapolations that need to be made with $\mathbf{V}_{m-1}$ is $k-m$.

To aid in understanding, an illustrative example is presented in Figs. 2–5 to demonstrate the principles of the CT-DMD model.

1) Initially, define a set of 2-D time-series data $\{\mathbf{x}_E(t_0), \mathbf{x}_E(t_1), \mathbf{x}_E(t_2)\}$ in the Eulerian coordinate system. Use the optical flow model to calculate

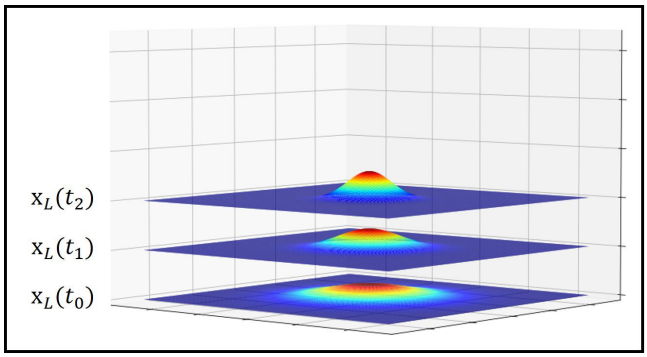

Fig. 3. Step 2 of illustrative example, time-series data in the Eulerian coordinate system are converted to the Lagrangian coordinate system by extrapolation using velocity fields.

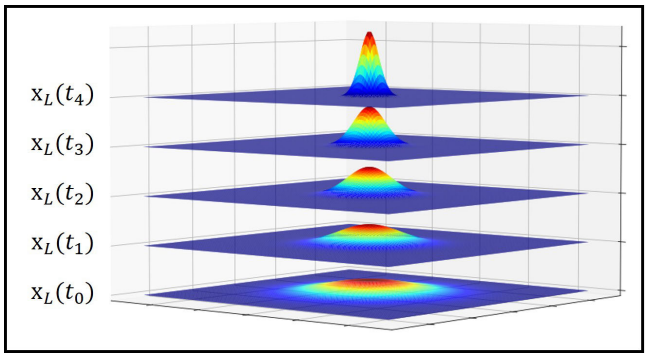

Fig. 4. Step 3 of illustrative example, by analyzing the time-series data in the Lagrangian coordinate system using the DMD model, forecasting can be made.

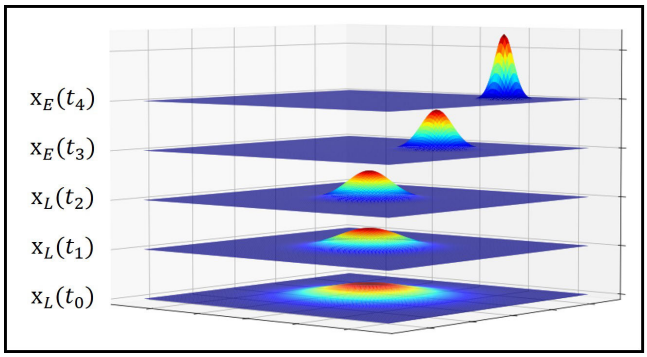

Fig. 5. Step 4 of illustrative example, time-series data forecast in the Lagrangian coordinate system are converted to the Eulerian coordinate.

velocity fields $\{\mathbf{V}_0, \mathbf{V}_1\}$ between $\{\mathbf{x}_E(t_0), \mathbf{x}_E(t_1)\}$ and $\{\mathbf{x}_E(t_1), \mathbf{x}_E(t_2)\}$, as shown in Fig. 2.

2) Time-series data $\{\mathbf{x}_E(t_0), \mathbf{x}_E(t_1), \mathbf{x}_E(t_2)\}$ in the Eulerian coordinate system are converted to $\{\mathbf{x}_L(t_0), \mathbf{x}_L(t_1), \mathbf{x}_L(t_2)\}$ in the Lagrangian coordinate system by extrapolation using velocity fields $\{\mathbf{V}_0, \mathbf{V}_1\}$. Here, the reference time point is t_2, as shown in Fig. 3.
3) By analyzing $\{\mathbf{x}_L(t_0), \mathbf{x}_L(t_1), \mathbf{x}_L(t_2)\}$ using the DMD model, forecasting can be made for $\{\mathbf{x}_L(t_3), \mathbf{x}_L(t_4)\}$, as shown in Fig. 4.
4) Time-series data $\{\mathbf{x}_L(t_3), \mathbf{x}_L(t_4)\}$ in the Lagrangian coordinate system are converted to $\{\mathbf{x}_E(t_3), \mathbf{x}_E(t_4)\}$ in the Eulerian coordinate by extrapolation using velocity field $\mathbf{V}_1$, as shown in Fig. 5.

III. Model Validation

In this study, we evaluate the validity of the CT-DMD model for rainfall forecasting using the Rainymotion model as a benchmark.

A. Data

The rainfall data used in this study were collected from the Kanto region of Japan in August 2015 and August 2017 at a temporal resolution of 1 min using X-band MP radar data [46]. The original data have a grid size of [800, 800], where each grid cell measures 250 × 250 m. To enhance computational efficiency, we applied downsampling by using the mean function on local blocks. The downscaled data have a grid size of [200, 200], corresponding to an actual size of 200 × 200 km, with each grid cell measuring 1 × 1 km.

Based on the findings presented in [47], which revealed the presence of seemingly random sampling containing hidden biases and errors, in this study, we employed the method of downsampling using the mean function on local blocks. This downsampling method comprises three steps. In the first step, 2-D data are segmented into smaller, nonoverlapping blocks of the same size; in the second step, the mean value of each block is calculated; and in the third step, this mean value is used to represent the entire block. In essence, this downsampling method is analogous to the commonly used technique in machine learning known as average pooling. This method aims to achieve a better balance between enhancing computational efficiency and lowering spatial resolution of data. In this study, to enhance computational efficiency, we applied this downsampling method to reduce the spatial resolution of rainfall data. However, for forecasting purposes, a resolution of 1 × 1 km still falls within an acceptable range.

The shape of the collected dataset was [h, min, size_y, size_x]. To ensure that there was sufficient rainfall for model evaluation, the data from the 29th min of each hour were examined. If the area of rainfall in this 29th min of data was greater than one-third of the data size, the 60 min of data from that particular hour was filtered and included as a subset in the experimental dataset.

After filtering, the final experimental dataset had the shape of [h, min, size_y, size_x] = [45, 60, 200, 200], that is, 45 h of data was filtered. The "hours" component has a size of 45, ranging from 0 to 44. The "minutes" component has a size of 60, ranging from 0 to 59. Both the "size" components have a size of 200, ranging from 0 to 199. Fig. 6 shows the sample data.

In addition, in this study, all data are in the Eulerian coordinate system, that is, at a fixed range of latitude and longitude.

B. CT-DMD Model Implementation Process

We defined each hour of data in the experimental dataset as a subset, and 0–30 min of each subset was designated as the input data for the CT-DMD model. Moreover, 30–59 min of each subset was designated as the target data for assessing the accuracy of the model.

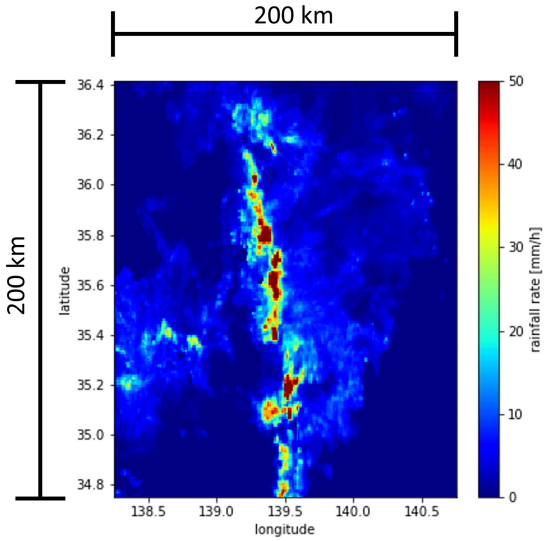

Fig. 6. Horizontal coordinates represent the longitude, the vertical coordinates represent the latitude, and the rainfall rate is visualized using a color bar ranging from 0 to 50 mm/h.

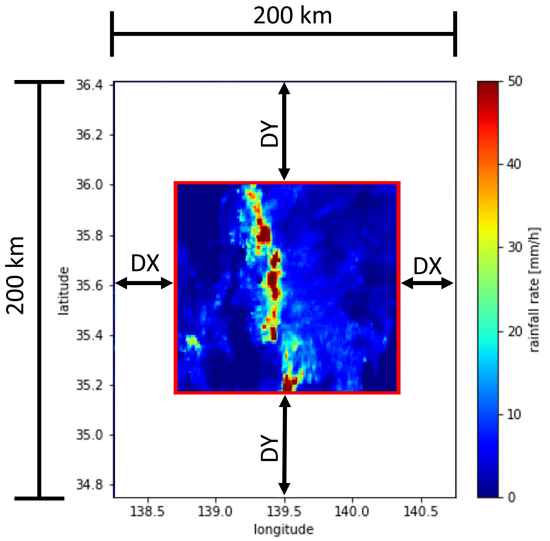

Fig. 7. DY is the maximum displacement of rainfall in the vertical coordinate over the 0–30-min time range and DX is the maximum displacement of rainfall in the horizontal coordinate over the 0–30-min time range.

The CT-DMD model performs the following forecasting process for each subset.

1) The velocity field between each pair of adjacent data is calculated using the DIS optical flow model over the time range of 0–30 min $\{\mathbf{x}_E(t_0), \mathbf{x}_E(t_1), \mathbf{x}_E(t_2), \ldots, \mathbf{x}_E(t_{30})\}$

$$\mathbf{V}_k = \text{DIS Optical Flow}(\mathbf{x}_E(t_k), \mathbf{x}_E(t_{k+1})) \times (k = 0, \ldots, 29).$$

2) Velocity fields $\{\mathbf{V}_0, \mathbf{V}_1, \mathbf{V}_2, \ldots, \mathbf{V}_{29}\}$ are used to convert the data from 0 to 30 min to those in the Lagrangian coordinate system $\{\mathbf{x}_L(t_0), \mathbf{x}_L(t_1), \mathbf{x}_L(t_2), \ldots, \mathbf{x}_L(t_{30})\}$ with the reference time point of the 30th min

$$\mathbf{x}_L(t_k) = \text{Convert}_{EL}(\mathbf{x}_E(t_k), \{\mathbf{V}_k, \mathbf{V}_{k+1}, \ldots, \mathbf{V}_{29}\}) \times (k = 0, \ldots, 29).$$

$\mathbf{x}_E(t_{30})$ is equal to $\mathbf{x}_L(t_{30})$, and no conversion is needed. In this study, Convert_{EL} consists of two operations: extrapolation of the data using a backward constant-vector scheme and interpolation of the extrapolated data using the nearest method.

3) Because the original data are in the Eulerian coordinate system, the latitude and longitude range of the data is fixed. Thus, as time progresses, rainfall outside the data region may enter the data region. To mitigate the impact of rainfall outside the designated region on the model performance, we apply region trimming to the data in the Lagrangian coordinate system.
We define the maximum displacement of rainfall along the vertical and horizontal coordinates in the time range of 0–30 min as DY and DX, respectively. DY and DX are calculated using the DIS optical flow. Incidentally, DY and DX of each subset are not consistent.
Next, we trim the region of data from [0 to 200, 0 to 200] to [DY to 200-DY, DX to 200-DX], as shown in Fig. 7.

4) We divide the trimmed data into two parts: [0, 29] and [1, 30] min and then combine them along the vertical axis

$$\mathbf{X}_{LP} = \begin{bmatrix} \mathbf{x}_L(t_0) & \mathbf{x}_L(t_1) & \mathbf{x}_L(t_2) & \cdots & \mathbf{x}_L(t_{29}) \\ \mathbf{x}_L(t_1) & \mathbf{x}_L(t_2) & \mathbf{x}_L(t_3) & \cdots & \mathbf{x}_L(t_{30}) \end{bmatrix}.$$

Based on our testing, this is a helpful strategy to improve the accuracy of forecasts. We define the data processed in the Lagrange coordinate system as $\{\mathbf{x}_{LP}(t_0), \mathbf{x}_{LP}(t_1), \mathbf{x}_{LP}(t_2), \ldots, \mathbf{x}_{LP}(t_{29})\}$.

5) Processed data in the Lagrangian coordinate system $\{\mathbf{x}_{LP}(t_0), \mathbf{x}_{LP}(t_1), \mathbf{x}_{LP}(t_2), \ldots, \mathbf{x}_{LP}(t_{29})\}$ are analyzed using the DMD. The analyzed DMD modes Φ and DMD eigenvalues Λ are then used to forecast data $\{\mathbf{x}_{LP}(t_{30}), \mathbf{x}_{LP}(t_{31}), \mathbf{x}_{LP}(t_{32}), \ldots, \mathbf{x}_{LP}(t_{59})\}$

$$\mathbf{x}_{LP}(t_k) = \Phi \Lambda^k \Phi^\dagger \mathbf{x}_{LP}(t_0) = \sum_{i=1}^{M} \phi_i \lambda_i^k \phi_i^\dagger \mathbf{x}_{LP}(t_0) \times (k = 30, \ldots, 59)$$

$$\mathbf{X}_{LP} = \begin{bmatrix} \mathbf{x}_L(t_{30}) & \mathbf{x}_L(t_{31}) & \mathbf{x}_L(t_{32}) & \cdots & \mathbf{x}_L(t_{59}) \\ \mathbf{x}_L(t_{31}) & \mathbf{x}_L(t_{32}) & \mathbf{x}_L(t_{33}) & \cdots & \mathbf{x}_L(t_{60}) \end{bmatrix}.$$

6) Due to previous data processing, we only take the upper half of the forecast data along the vertical axis. Because the forecast values are complex numbers, we only take the real part

$$\mathbf{X}_L = \begin{bmatrix} \mathbf{x}_L(t_{30}) & \mathbf{x}_L(t_{31}) & \mathbf{x}_L(t_{32}) & \cdots & \mathbf{x}_L(t_{59}) \end{bmatrix}.$$

7) Finally, using the $\mathbf{V}_{29}$ velocity field, the data in the Lagrangian coordinate system are converted back to those in the Eulerian coordinate system

$$\mathbf{x}_E(t_k) = \text{Convert}_{LE}(\mathbf{x}_L(t_k), \{V_{29}, V_{29}, \ldots, V_{29}\}) \times (k = 30, \ldots, 59).$$

The number of extrapolations that need to be made with $\mathbf{V}_{29}$ is $k - 30$. In this study, Convert_{LE} consists of

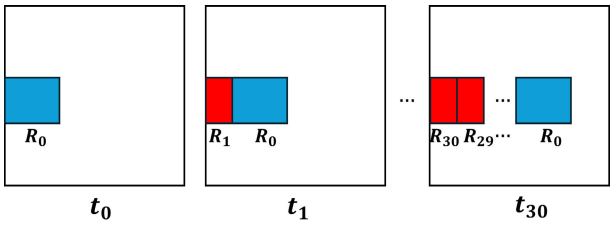

Fig. 8. Simple input data (0–30 min) example of rainfall, $\mathbf{t}_n$ indicates the data at time point n, and $\mathbf{R}_n$ represents the rainfall points that are present in the input data starting from time point n.

two operations: extrapolation of the data using a backward constant-vector scheme and interpolation of the extrapolated data using the inverse distance weighting method.

In the implementation stage, owing to the characteristics of the rainfall data, the CT-DMD model has an additional data-trimming step. Furthermore, to enhance the accuracy, we include a data combination step.

Solely as a reference, in this study, the CT-DMD model takes only about 12 s to implement for each subset, and the computer's CPU and GPUs used for this research are the 12th Gen Intel[1] Core[2] i5-12450H CPU, NVIDIA GeForce RTX 4050 Laptop GPU, and Intel[1] UHD Graphics GPU. For real-time forecasting, we consider this time to be sufficiently fast.

C. Explanation of Data-Trimming Step

Regarding the necessity of the data-trimming step, we can explain it from two perspectives. The first is to ensure the time completeness of rainfall points in the Lagrangian coordinate system. The second is to evaluate the accuracy of each model more precisely.

1) To Ensure the Time Completeness of Rainfall Points: For explanatory purposes, we assume a simple input data (0–30 min) example of rainfall moving from left to right, as shown in Fig. 8. The data ranging from 0 to 30 min of each subset was designated as the input data for the CT-DMD model. $\mathbf{t}_n$ indicates the data at time point n, and $\mathbf{R}_n$ represents the rainfall points that are present in the input data starting from time point n. It can be observed that at $\mathbf{t}_0$, only $\mathbf{R}_0$ is present within the input data, and at $\mathbf{t}_1$, the rainfall moves to the right, introducing $\mathbf{R}_1$ into the input data. Furthermore, with each subsequent time step $\mathbf{t}_n$, a new $\mathbf{R}_n$ will be incorporated into the input data until $\mathbf{t}_{30}$.

As shown in Fig. 9, these rainfall points $\mathbf{R}_n(0 < n)$ that enter the input data after $\mathbf{t}_0$ will have a partial absence of time in the input data. It can be observed that $\mathbf{R}_0$ is present in the input data from $\mathbf{t}_0$, so its time presence in the input data is complete. However, $\mathbf{R}_1$ enters the input data from $\mathbf{t}_1$, resulting in its time presence in the input data missing the portion corresponding to $\mathbf{t}_0$; and each $\mathbf{R}_n(0 < n)$ entering the input data after $\mathbf{t}_0$ will lack the portion of time from $\mathbf{t}_0$ to $\mathbf{t}_{n-1}$.

In the Lagrangian coordinate system, these rainfall points $\mathbf{R}_n(0 < n)$, lacking time completeness, will suddenly appear at time $\mathbf{t}_n$ in the input data, which clearly does not align with the reality of rainfall event. In order to mitigate the impact of these rainfall points $\mathbf{R}_n(0 < n)$ on the analysis of the DMD model, we used data trimming to remove this portion of rainfall points $\mathbf{R}_n(0 < n)$.

[1]Registered trademark.
[2]Trademarked.

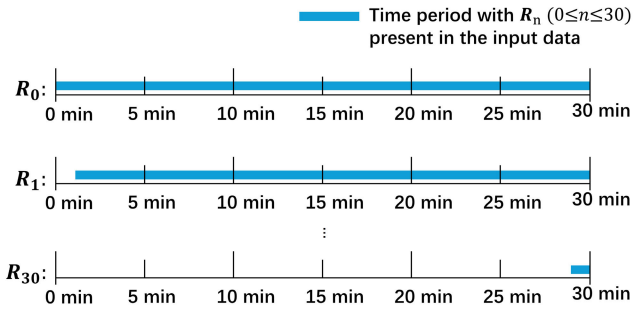

Fig. 9. Blue line represents the time period with $\mathbf{R}_n(0 \le n \le 30)$ present in the input data.

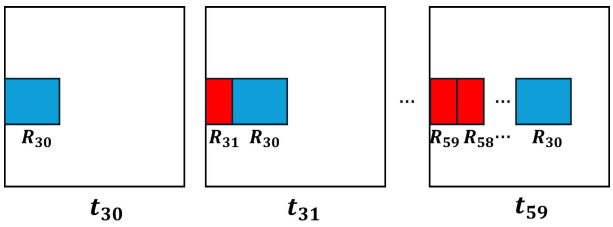

Fig. 10. Simple data (30–59 min) example of rainfall, $\mathbf{t}_n$ indicates the data at time point n, and $\mathbf{R}_n$ represents the rainfall points that are present in the data starting from time point n.

2) To Evaluate the Accuracy of Each Model More Precisely: For explanatory purposes, we assume a simple data (30–59 min) example of rainfall moving from left to right, as shown in Fig. 10. The data ranging from 30 to 59 min of each subset was designated as the target data for assessing the accuracy of each model. $\mathbf{t}_n$ indicates the data at time point n, and $\mathbf{R}_n$ represents the rainfall points that are present in the data starting from time point n. It can be seen that as the time step increases, rainfall points $\mathbf{R}_n(30 < n)$ outside the range of the data will enter into the data. For both the CT-DMD model and the Rainymotion model, it is difficult to use rainfall points within the data range to forecast rainfall points outside the data range. Therefore, in order to mitigate the impact of rainfall points $\mathbf{R}_n(30 < n)$, which are outside the data range, on the model's accuracy evaluation, we have also restricted the evaluation accuracy within the range after the data-trimming step.

D. Results

Because the values of DY and DX were different for each subset, the data sizes of the forecast results were also different for each subset. To unify the size of the forecast results when evaluating forecasting accuracy, we chose the maximum DY and DX as the unified trimmed values, where DY and DX are 57 and 32 km, respectively. This suggests that the region for evaluation accuracy is a rectangle of 86 × 136 km, as shown in Fig. 11. We consider this size sufficient for the objective evaluation of accuracy.

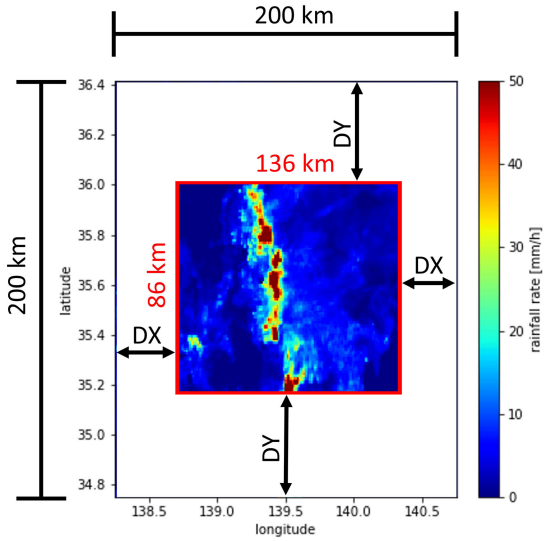

Fig. 11. DY and DX are 57 and 32 km, respectively, and the region for accuracy evaluation is a rectangle of 86 × 136 km.

We employed the root mean square error (RMSE) and mean square error (MSE)-based skill scores [48] and Nash–Sutcliffe model efficiency (NSE) coefficient [49] as the performance metrics to evaluate the following models.

1) *CT-DMD Model:* The model proposed in this study.
2) *Rainymotion Model:* The rainfall forecasting model is constructed on the basis of the optical flow model.
3) *DMD Model:* The data-driven model developed recently is a part of the CT-DMD model. The forecast data are obtained by using the DMD eigenvalues and DMD modes of the input data.
4) *Persistence Model:* The model assumes that rainfall distribution remains constant. It assumes that all forecast data remain consistent with the value of $\mathbf{x}_E(t_{30})$.

The forecast data range for each subset was 30–59 min.

1) Root Mean Square Error:

$$\mathrm{RMSE} = \frac{1}{H}\sum_{h}\sqrt{\frac{\sum_{y,x}(F(h,m,y,x)-T(h,m,y,x))^2}{N}} \tag{1}$$

where the variables are defined as follows.

1) F is the forecast data.
2) T is the target data.
3) N is the total number of grids of each forecast data $N = 86 \times 136$.
4) y and x are the coordinates of each forecast data $57 \leq y \leq 142$, $32 \leq x \leq 167$.
5) H is the total number of hours of the experimental dataset $H = 45$.
6) h is an hour within H, $0 \leq h \leq 44$.
7) m is a minute within h, $30 \leq m \leq 59$.

As shown in (1), we performed RMSE error calculations between the target and forecast data at each hour and minute and then averaged them in the "hour" dimension.

The results are presented in Fig. 12. Among all models, the proposed CT-DMD model exhibited the lowest error after a lead time of 10 min. At the lead time of 0 min, which corresponds to forecast data $\mathbf{x}_E(t_{30})$, the errors of the Rainymotion and persistence models are 0 mm/h, whereas the CT-DMD and DMD models exhibit nonzero errors. This is because the Rainymotion and persistence models utilize extrapolation or consistency with $\mathbf{x}_E(t_{30})$ to generate the forecast data, while the CT-DMD and DMD models employ DMD modes and DMD eigenvalues to reconstruct the nonlinear data from $\mathbf{x}_L(t_{30})$ to $\mathbf{x}_L(t_{59})$, followed by extrapolation. Therefore, the error of the Rainymotion model was lower than that of the CT-DMD model when the rainfall had not yet changed significantly. However, after a lead time of 10 min, the CT-DMD model, which can analyze changes in the rainfall rate, has much lower errors than the Rainymotion model.

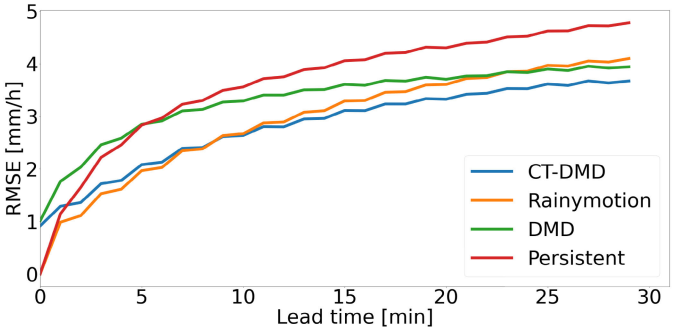

Fig. 12. RMSE calculated between the forecast data of each model and target data.

2) MSE-Based Skill Scores:

$$\text{Skill Score}_{\mathrm{MSE}} = 1 - \frac{\mathrm{MSE}(f,t)}{\mathrm{MSE}(r,t)} \tag{2}$$

where the variables are defined as follows.

1) f(forecast) is the forecast data generated by the CT-DMD model.
2) r(reference) is the forecast data generated by the Rainymotion model.
3) t is the target data.

Murphy [48] proposed the skill scores based on MSE. These scores effectively allow performance comparison between the two models. Equation (2) shows that when the skill score is positive, the error of the CT-DMD model is lower than that of the Rainymotion model. Moreover, when the skill score is negative, the error of the CT-DMD model is higher than that of the Rainymotion model. The values for the skill score ranged from negative to 1.

We used (2) to perform the calculations between the target data and the forecast data generated by the CT-DMD/Rainymotion model for each hour and minute and then averaged them in the "hour" dimension.

The results are presented in Fig. 13. At the lead time of 0 min, that is, at $\mathbf{x}_E(t_{30})$, the forecast generated by the Rainymotion model is perfect, resulting in a skill score of negative infinity. At the lead time of 5–10 min, the skill scores become positive, which indicates that the CT-DMD model showed lower errors than the Rainymotion model. As the lead time increases, the CT-DMD model shows an increasingly clear accuracy advantage over the Rainymotion model.

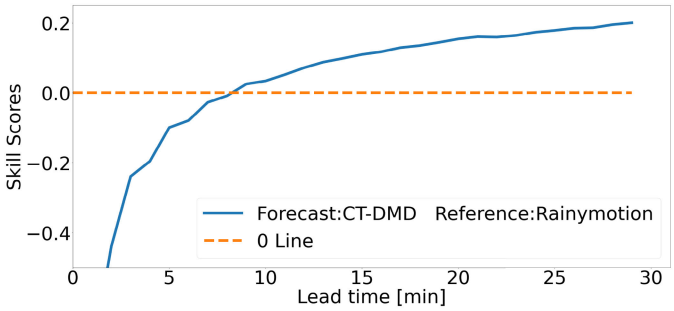

Fig. 13. MSE-based skill scores calculated from the forecast results of the CT-DMD/Rainymotion model and target data.

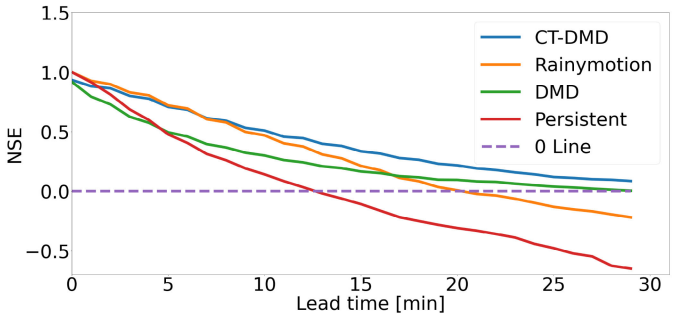

Fig. 14. NSE calculated between the forecast data of each model and target data.

3) Nash–Sutcliffe Model Efficiency:

$$\mathrm{NSE}(h,m) = 1 - \frac{\sum_{y,x}(T(h,m,y,x) - F(h,m,y,x))^2}{\sum_{y,x}\left(T(h,m,y,x) - \overline{T(h)}\right)^2} \tag{3}$$

$$\mathrm{NSE}(m) = \frac{1}{H}\sum_{h}\mathrm{NSE}(h,m) \tag{4}$$

where the variables are defined as follows.

1) F is the forecast data.
2) T is the target data.
3) y and x are the coordinates of each forecast data $57 \leq y \leq 142$, $32 \leq x \leq 167$.
4) H is the total number of hours of the experimental dataset $H = 45$.
5) h is an hour within H, $0 \leq h \leq 44$.
6) m is a minute within h, $30 \leq m \leq 59$.

NSE is one of the common performance evaluation metrics for hydrological models, with a value range from negative to 1, and a greater NSE value indicates better forecast performance of the model. As shown in (3), it can be observed that the NSE can be employed to assess the forecast performance of the model compared to the baseline from the perspective of the sum of squared errors, where the baseline is commonly selected as the mean value of the target data. Therefore, in this article, we select the baseline as the mean value of the target data in each subset, defined as $\overline{T(h)}$. When the NSE > 0, it suggests that the model's forecast performance is better than $\overline{T(h)}$. Conversely, when the NSE < 0, it suggests that the model's forecast performance is worse than $\overline{T(h)}$. We calculated the NSE between the forecast data of each model and target data for each hour and minute, as shown in (3). Then, averaged them along the "hour" dimension, as shown in (4).

The results are presented in Fig. 14, it can be observed that because the Rainymotion model and the persistent model utilize extrapolation or consistency with $\mathbf{x}_E(t_{30})$ to generate the forecast data, the NSE values of these two models are both equal to 1 at the lead time of 0 min. However, as the lead time increases, the CT-DMD model, which can analyze changes in the rainfall rate, gradually demonstrates greater NSE values than the Rainymotion model. Furthermore, it can be observed that at the lead time of 20–25 min, the NSE value of the Rainymotion model starts to become less than 0, indicating that the forecast performance of the Rainymotion model becomes lower than $\overline{T(h)}$. However, the NSE value of the CT-DMD model remains greater than 0 throughout, indicating that the forecast performance of the CT-DMD model consistently exceeds $\overline{T(h)}$.

4) Forecasting Results: Fig. 15 shows the forecast results for each model; the data are the 22nd subset from the experimental dataset, and the forecast characteristics of each model can be seen. The Rainymotion model can capture atmospheric motion but cannot analyze and forecast rainfall intensity variations. In contrast, the DMD model is capable of analyzing and forecasting rainfall intensity variations but cannot capture atmospheric motion. The proposed CT-DMD model combines the advantages of both models and can analyze and forecast atmospheric motion and rainfall intensity variation simultaneously.

IV. Discussion

Fig. 16 presents the MSE-based skill scores [see 2] for each subset of the experimental dataset. After a lead time of 15 min, the CT-DMD model was found to be more accurate (with lower errors) than the Rainymotion model in most subsets.

When the lead time is 5 min, ten subsets of the experimental dataset have positive skill scores and 35 subsets have negative skill scores, that is, 22.22% of the subsets in the experimental dataset show that the CT-DMD model exhibits a higher forecast accuracy than the Rainymotion model. When the lead time is 15 min, 31 subsets of the experimental dataset have positive skill scores and 14 subsets have negative skill scores, that is, 68.89% of the subsets in the experimental dataset show that the CT-DMD model exhibits a higher forecast accuracy than the Rainymotion model. When the lead time is 25 min, 40 subsets of the experimental dataset have positive skill scores and five subsets have negative skill scores, that is, 88.89% of the subsets in the experimental dataset show that the CT-DMD model exhibits a higher forecast accuracy than the Rainymotion model. As the lead time increases, the CT-DMD model shows an increasingly clear accuracy advantage over the Rainymotion model.

The abovementioned results are summarized in Table I, where SS(positive) is the number of subsets with positive skill scores, SS(negative) is the number of subsets with negative skill scores, and SS(positive)% is the number of subsets

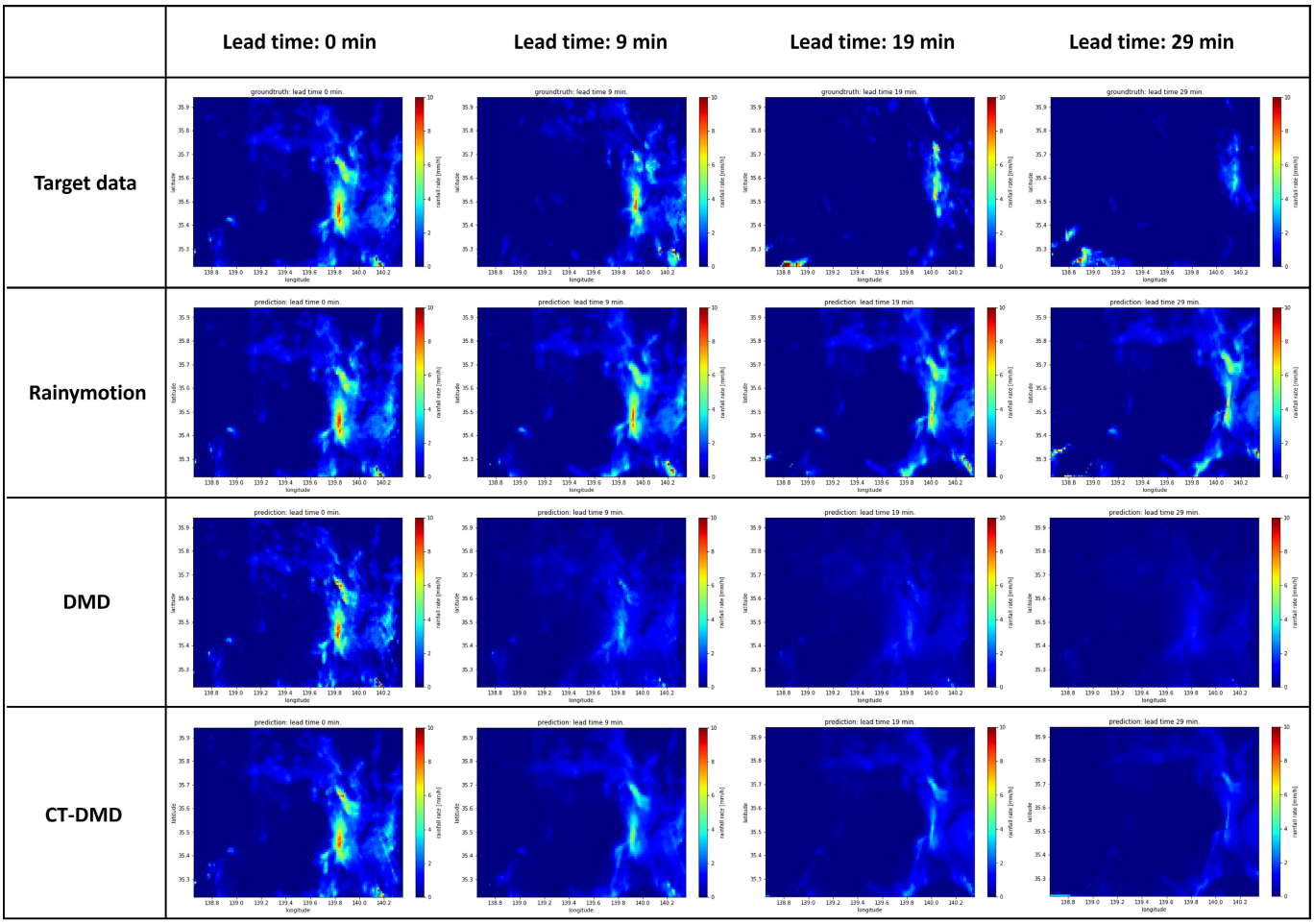

Fig. 15. Forecasting results of each model in dataset 22. The rainfall rate is visualized using a color bar ranging from 0 to 10 mm/h.

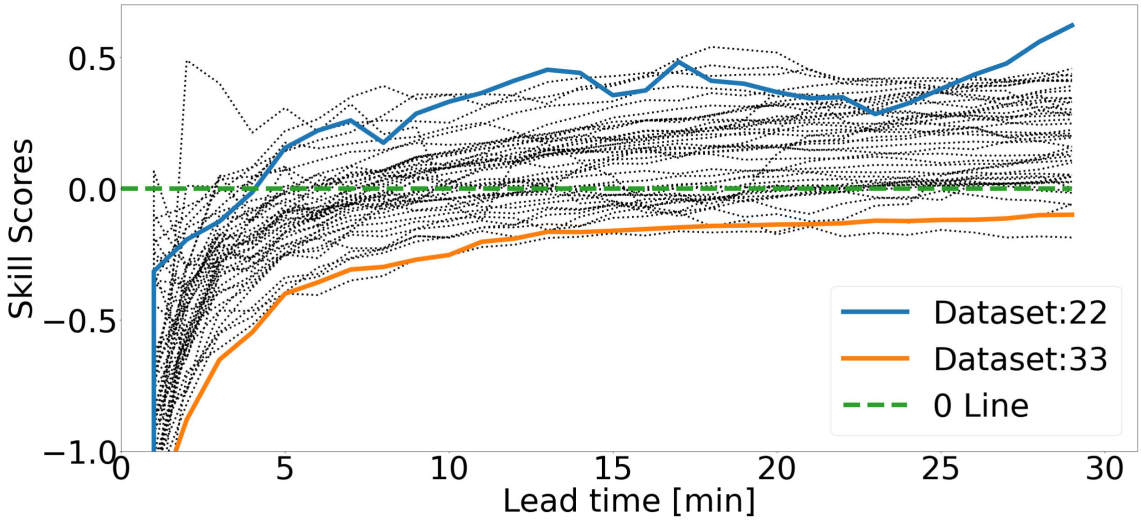

Fig. 16. MSE-based skill scores for each subset in the experimental dataset.

with positive skill scores as a percentage of the experimental dataset.

Here, we introduce the relative bias [50] between the forecast data of the Rainymotion model and the target data as a new topic for discussion

$$\text{Relative Bias} = \frac{\sum_{y,x}(F(h,m,y,x) - T(h,m,y,x))}{\sum_{y,x} T(h,m,y,x)} \quad (5)$$

TABLE I
STATISTICAL ANALYSIS OF THE MSE-BASED SKILL SCORES ACROSS ALL SUBSETS

Lead time	5 min	15 min	25 min
SS(positive)	10	31	40
SS(negative)	35	14	5
SS(positive)%	22.22%	68.89%	88.89%

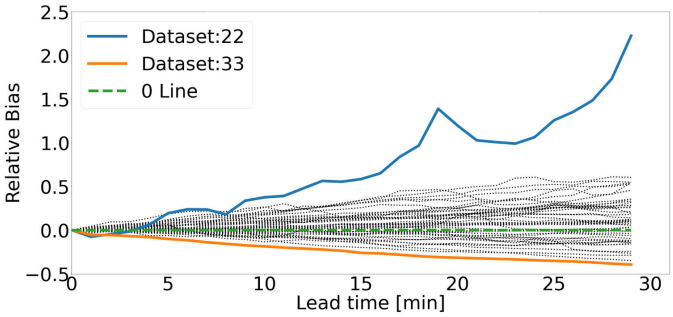

Fig. 17. Relative bias between the forecast data of the Rainymotion model and target data in all subsets.

where the variables are defined as follows.

1) F is the forecast data.
2) T is the target data.
3) y and x are the coordinates of each forecast data $57 \leq y \leq 142$, $32 \leq x \leq 167$.
4) H is the total number of hours of the experimental dataset $H = 45$.
5) h is an hour within H, $0 \leq h \leq 44$.
6) m is a minute within h, $30 \leq m \leq 59$.

As described in (5), the relative bias calculation demonstrates the disparity between the forecast and target data. When the relative bias is positive, it indicates that the forecast data are greater than the target data, and when the relative bias is negative, it indicates that the forecast data are less than the target data; a smaller absolute value of the relative bias indicates a smaller disparity between the forecast and target data.

Furthermore, assuming that the Rainymotion model can perfectly analyze and forecast atmospheric motion and by utilizing the inherent characteristic of the Rainymotion model that maintains constant rainfall intensity in the forecast data [7], we can determine whether rainfall is growing or declining by examining the relative bias between the forecast data of the Rainymotion model and target data. A positive and increasing relative bias indicates a declining rainfall trend in the target data, whereas a negative and decreasing relative bias suggests a growing rainfall trend in the target data.

A. Growing/Declining Trend in Target Data

Fig. 17 shows the relative bias between the forecast data of the Rainymotion model and target data for all subsets. We divided all the relative bias curves into two groups with increasing trend (Fig. 18) and decreasing trend (Fig. 19). The increasing group had 29 subsets, while the decreasing group had 16 subsets. The relative bias curves with an increasing

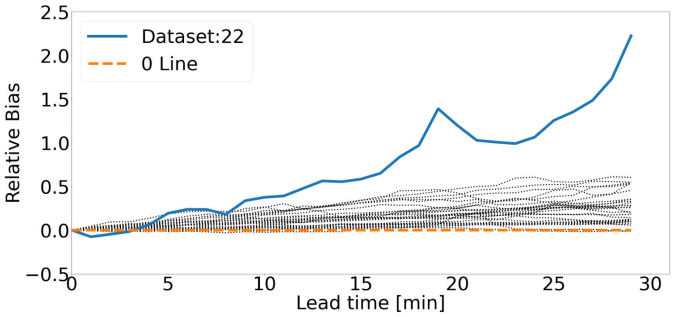

Fig. 18. Relative bias curves with an increasing trend.

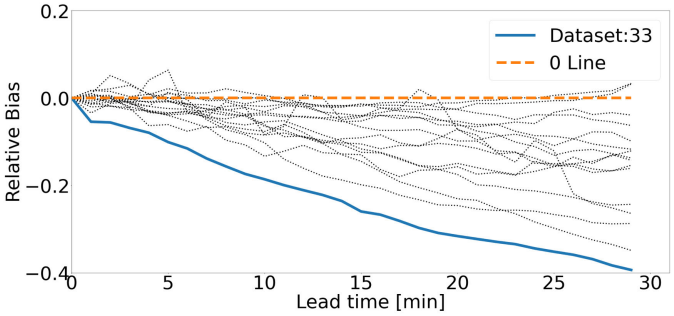

Fig. 19. Relative bias curves with a decreasing trend.

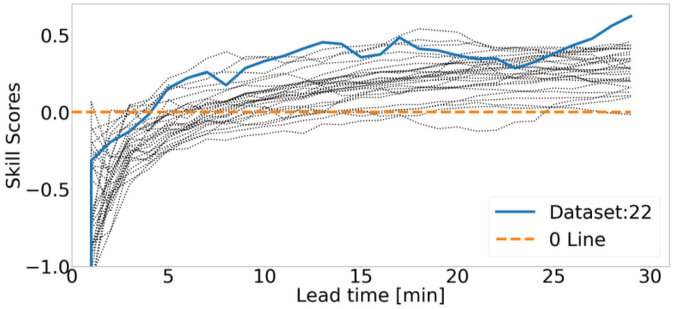

Fig. 20. Skill scores for the subsets of the relative bias curves with an increasing trend.

trend represent a declining tendency in the target data, and the relative bias curves with a decreasing trend represent a growing tendency in the target data. Fig. 20 shows the skill scores of the CT-DMD model for subsets of the relative bias curves with an increasing trend and Fig. 21 shows the skill scores of the CT-DMD model for subsets of the relative bias curves with a decreasing trend; the skill scores are calculated, and the parameters are chosen as in (2).

For the relative bias curves with an increasing trend (the target data with a declining trend), when the lead time is 5 min, eight subsets of the increasing group have positive skill scores and 21 subsets have negative skill scores, that is, 27.59% of the subsets in the increasing group show that the CT-DMD model exhibits a higher forecast accuracy than the Rainymotion model. When the lead time is 15 min, 27 subsets of the increasing group have positive skill scores and two subsets have negative skill scores, that is, 93.1% of the subsets in the increasing group show that the CT-DMD model exhibits a higher forecast accuracy than the Rainymotion model. When the lead time is 25 min, 29 subsets of the increasing group have

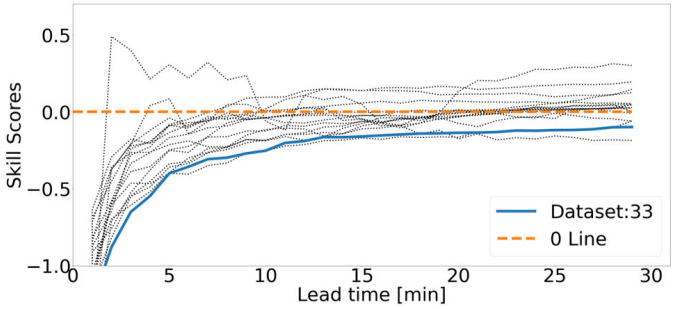

Fig. 21. Skill scores for the subsets of the relative bias curves with a decreasing trend.

TABLE II
RELATIVE BIAS CURVES WITH AN INCREASING TREND

Lead time	5 min	15 min	25 min
SS(positive)	8	27	29
SS(negative)	21	2	0
SS(positive)%	27.59%	93.1%	100%

TABLE III
RELATIVE BIAS CURVES WITH A DECREASING TREND

Lead time	5 min	15 min	25 min
SS(positive)	2	4	11
SS(negative)	14	12	5
SS(positive)%	12.5%	25%	68.75%

positive skill scores and zero subset has negative skill scores, that is, 100% of the subsets in the increasing group show that the CT-DMD model exhibits a higher forecast accuracy than the Rainymotion model. These results are summarized in Table II.

For the relative bias curves with a decreasing trend (target data with a growing trend), when the lead time is 5 min, two subsets of the decreasing group have positive skill scores and 14 subsets have negative skill scores, that is, 12.5% of the subsets in the decreasing group show that the CT-DMD model exhibits a higher forecast accuracy than the Rainymotion model. When the lead time is 15 min, four subsets of the decreasing group have positive skill scores and 12 subsets have negative skill scores, that is, 25% of the subsets in the decreasing group show that the CT-DMD model exhibits a higher forecast accuracy than the Rainymotion model. When the lead time is 25 min, 11 subsets of the decreasing group have positive skill scores and five subsets have negative skill scores, that is, 68.75% of the subsets in the decreasing group show that the CT-DMD model exhibits a higher forecast accuracy than the Rainymotion model. These results are summarized in Table III.

The CT-DMD model has a significantly superior forecasting capability to the Rainymotion model for the target data with a declining rainfall trend. However, for the target data with a growing trend, only 68.75% of the subsets demonstrated that the forecasting ability of the CT-DMD model surpassed that of the Rainymotion model when the lead time was 25 min.

V. CASE STUDY

In Figs. 16–21, we label the curves corresponding to the 22nd and 33rd subsets of the experimental dataset. It can be observed in Fig. 17 that the relative bias curve of the 22nd subset is the highest, indicating that the target data of the 22nd subset exhibit the maximum relative decrease trend in rainfall intensity among all the subsets. Conversely, the relative bias curve of the 33rd subset is the lowest, indicating that the target data of the 33rd subset exhibit the maximum relative increasing trend in rainfall intensity among all subsets. Fig. 16 shows that the skill score curve of the 22nd subset is one of the highest curves, indicating that the forecasting performance of the CT-DMD model in the 22nd subset is considerably higher than that of the Rainymotion model. Conversely, the skill score curve of the 33rd subset is one of the lowest, indicating that the forecasting performance of the CT-DMD model in the 33rd subset is considerably lower than that of the Rainymotion model. Because of the abovementioned particularities of the 22nd and 33rd subsets, we analyzed them in more depth to explore the reasons for the higher or lower forecasting performance of the CT-DMD model than that of the Rainymotion model.

Here, we introduce the relative bias of the trimmed input data and DMD eigenvalues as new topics for discussion.

By calculating the relative bias between trimmed input data $\mathbf{x}_L(t_0)$ and $\{\mathbf{x}_L(t_0), \mathbf{x}_L(t_1), \mathbf{x}_L(t_2), \ldots, \mathbf{x}_L(t_{30})\}$, the growing/declining trend of rainfall in the trimmed input data can be determined

$$\text{Relative Bias}_{(\text{trimmed input data})} = \frac{\text{sum}(\mathbf{x}_L(t_0) - \mathbf{x}_L(t_i))}{\text{sum}(\mathbf{x}_L(t_i))} \times (i = 0, \ldots, 30).$$

When the relative bias is positive and increasing, it indicates a declining trend in the trimmed input data. Conversely, when the relative bias is negative and decreasing, it indicates an increasing trend in the trimmed input data. The trimmed input data were obtained during the third step of the CT-DMD model implementation process.

The DMD eigenvalue is a complex value that represents the dynamic behavior of the corresponding DMD mode [38]. When the imaginary part of the DMD eigenvalue is nonzero, it indicates that the corresponding DMD mode exhibits oscillatory behavior. When the magnitude of the DMD eigenvalue was greater than 1, the corresponding DMD mode increased. Conversely, when the magnitude of the DMD eigenvalue was less than 1, the corresponding DMD mode decreased. The DMD eigenvalue is obtained in the fifth step of the CT-DMD model implementation process. The DMD eigenvalue allows the observation of the internal characteristics of the processed input data.

A. Dataset 22: CT-DMD Model Outperforms Rainymotion Model

In the 22nd subset of the experimental dataset, the forecasting performance of the CT-DMD model is significantly better than that of the Rainymotion model. Fig. 22 shows the relative

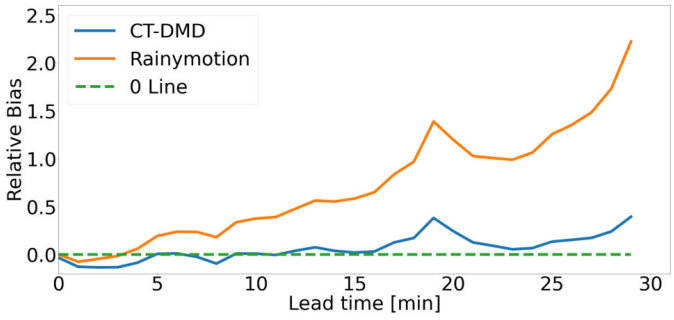

Fig. 22. Relative bias curve calculated from the forecast data of the Rainymotion/CT-DMD model and target data in dataset 22.

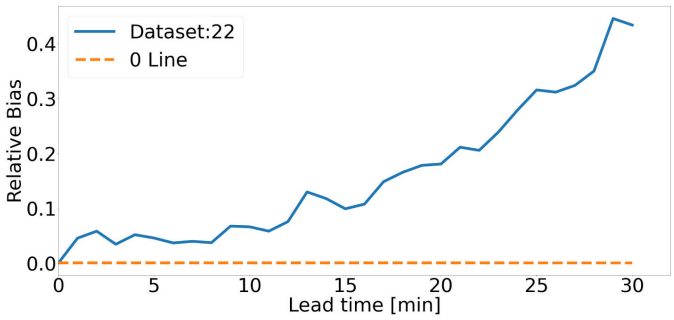

Fig. 23. Relative bias curve calculated from the trimmed input data $\mathbf{x}_L(t_0)$ and $\{\mathbf{x}_L(t_0), \mathbf{x}_L(t_1), \mathbf{x}_L(t_2), \ldots, \mathbf{x}_L(t_{30})\}$ in dataset 22.

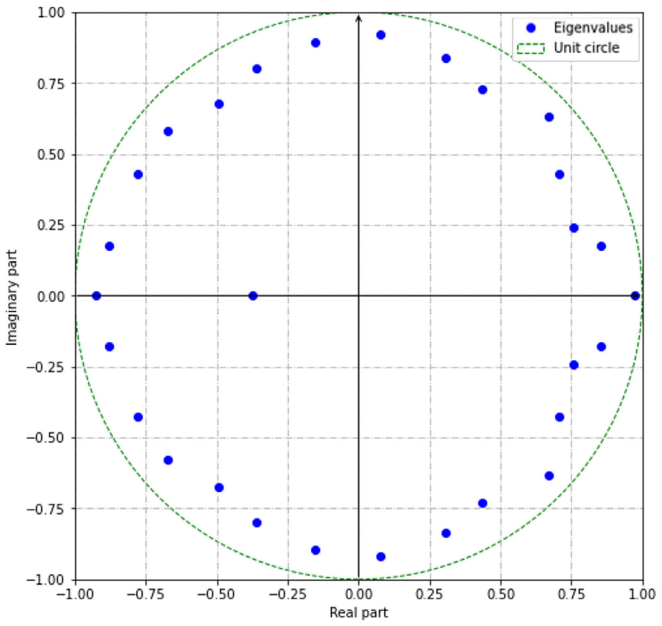

Fig. 24. DMD eigenvalues of the CT-DMD model in dataset 22. The horizontal axis is the real number axis, the vertical axis is the imaginary number axis, the blue dots are the DMD eigenvalues, and the green line is the unit circle.

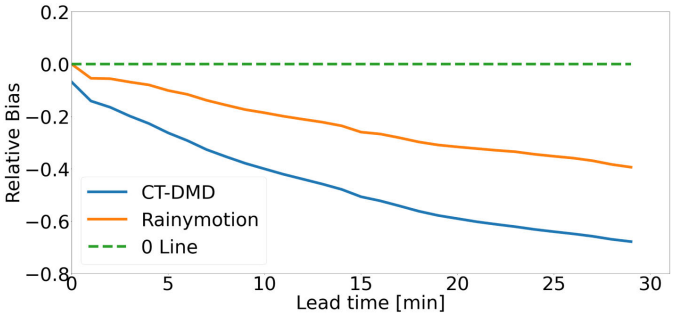

Fig. 25. Relative bias curve calculated from the forecast data of the Rainymotion/CT-DMD model and target data in dataset 33.

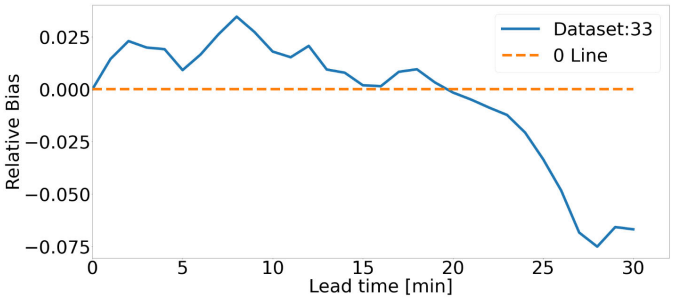

Fig. 26. Relative bias curve calculated from the trimmed input data $\mathbf{x}_L(t_0)$ and $\{\mathbf{x}_L(t_0), \mathbf{x}_L(t_1), \mathbf{x}_L(t_2), \ldots, \mathbf{x}_L(t_{30})\}$ in dataset 33.

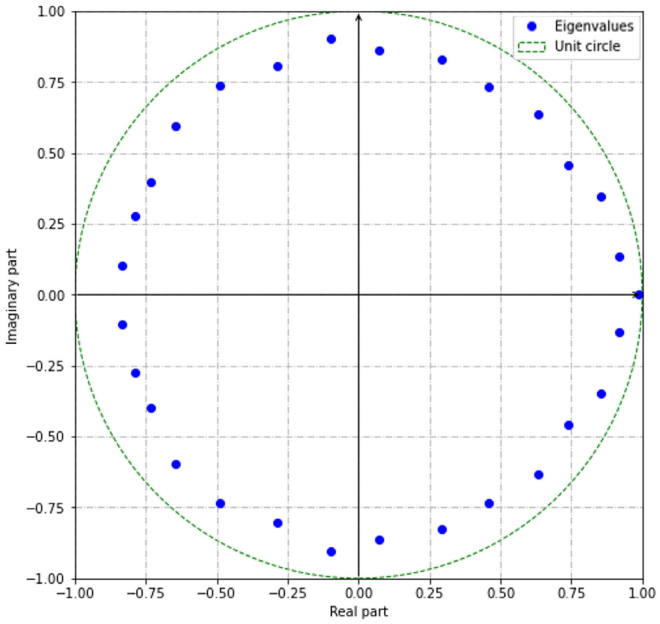

Fig. 27. DMD eigenvalues of the CT-DMD model in dataset 33. The horizontal axis is the real number axis, the vertical axis is the imaginary number axis, the blue dots are the DMD eigenvalues, and the green line is the unit circle.

bias curves between the forecast data of the Rainymotion/CT-DMD model and the target data in this subset. The relative bias curve of the Rainymotion model was positive and increasing, and the relative bias curve of the CT-DMD model remained nearly consistent with the 0 line. The positive and increasing relative bias curves of the Rainymotion model indicated a declining trend in the target rainfall data. Moreover, the relative bias curve of the CT-DMD model, which closely aligns with the 0 line, indicated that the forecast data of the CT-DMD model exhibit a declining trend similar to that of the target data. In addition, the relative bias curve of the CT-DMD model had a smaller absolute value than that of the Rainymotion model; therefore, the CT-DMD model performed better than the Rainymotion model for this subset.

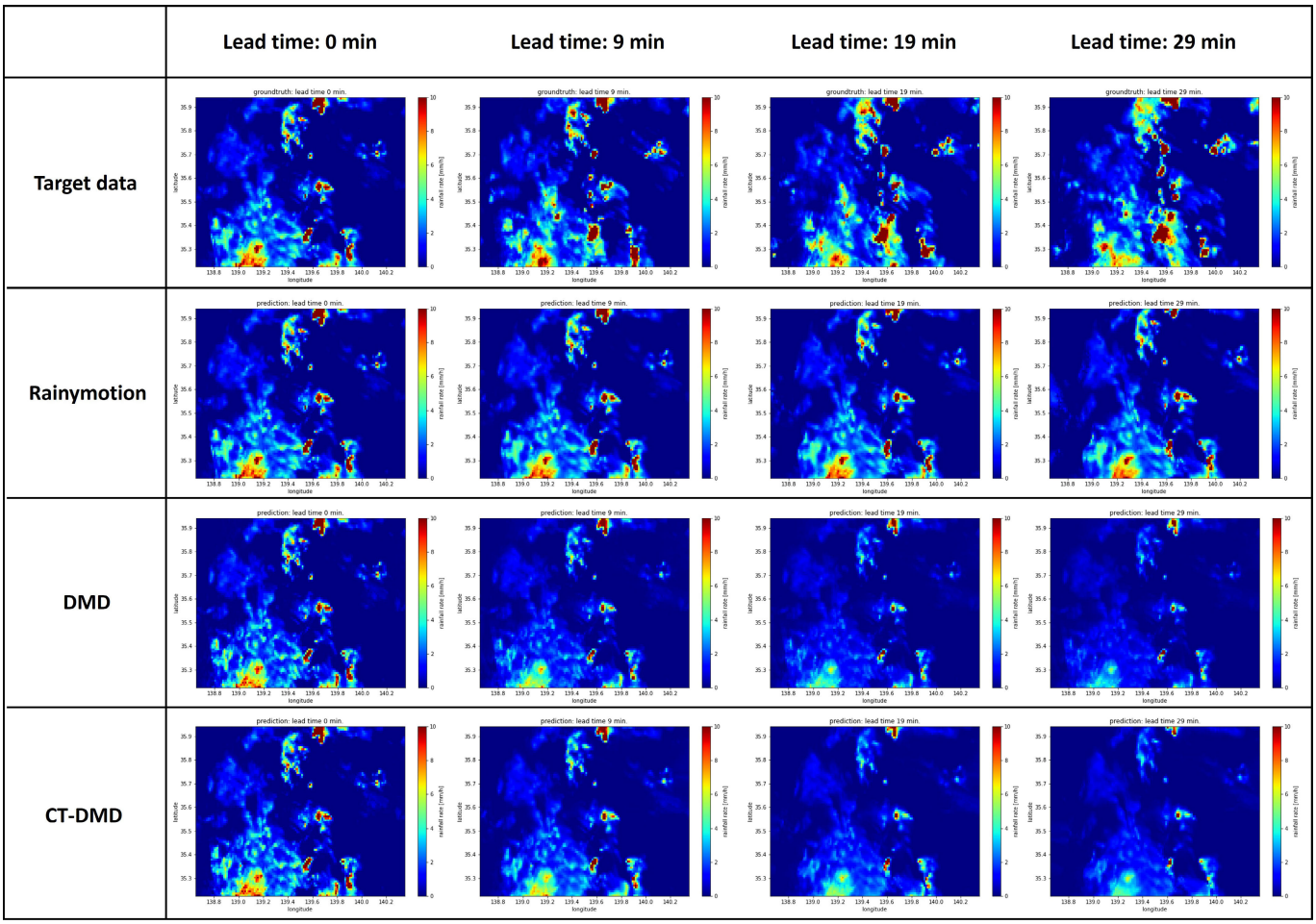

Fig. 28. Forecasting results of each model in dataset 33. The rainfall rate is visualized using a color bar ranging from 0 to 10 mm/h.

A visualization of the forecast data is shown in Fig. 15, which is consistent with our conclusions.

Fig. 23 shows the relative bias curve calculated from trimmed input data $\mathbf{x}_L(t_0)$ and $\{\mathbf{x}_L(t_0), \mathbf{x}_L(t_1), \mathbf{x}_L(t_2), \ldots, \mathbf{x}_L(t_{30})\}$ in this subset. The relative bias curve was positive and increasing, indicating a declining trend in the trimmed input data—this is also consistent with the fact that the magnitude of the DMD eigenvalues extracted from the processed input data is all less than 1, as shown in Fig. 24.

Therefore, owing to the similar variation (declining) trend between the input and target data, the CT-DMD model is capable of predicting good forecasts for this subset.

B. Dataset 33: CT-DMD Model Underperforms Rainymotion Model

In the 33rd subset of the experimental dataset, the forecasting performance of the CT-DMD model is lower than that of the Rainymotion model. Fig. 25 shows the relative bias curves between the forecast data of the Rainymotion/CT-DMD model and target data in this subset. The relative bias curves of the Rainymotion and CT-DMD models were negative and decreasing, but that of the CT-DMD model had a greater absolute value and greater downward trend. The negative and decreasing relative bias curve of the Rainymotion model indicated a growing trend in the target rainfall data. The relative bias curve of the CT-DMD model had a greater absolute value, and a greater downward trend indicated that the forecast data of the CT-DMD model have a declining trend. This misjudgment of rainfall trends resulted in lower accuracy of the CT-DMD model than that of the Rainymotion model for this subset.

A visualization of the forecast data is shown in Fig. 28, which is consistent with our conclusions.

Fig. 26 shows the relative bias calculated from the trimmed input data $\mathbf{x}_L(t_0)$ and $\{\mathbf{x}_L(t_0), \mathbf{x}_L(t_1), \mathbf{x}_L(t_2), \ldots, \mathbf{x}_L(t_{30})\}$ in this subset. The relative bias curve remained consistently positive until the lead time of 20 min. After a lead time of 20 min, the relative bias curve became negative and exhibited a decreasing trend. According to the DMD principle, the forecast data generated by the CT-DMD model rely on the initial state vector $\mathbf{x}_L(t_0)$, as shown in the following equation:

$$\mathbf{x}_L(t_k) = \Phi \Lambda^k \Phi^{\dagger} \mathbf{x}_L(t_0) = \sum_{i=1}^{M} \phi_i \lambda_i^k \phi_i^{\dagger} \mathbf{x}_L(t_0). \tag{6}$$

For $\mathbf{x}_L(t_0)$, the relative bias curve remained consistently positive before a lead time of 20 min, indicating a declining and oscillating rainfall trend in the trimmed input data. After a lead time of 20 min, the relative bias curve started to become

negative with a decreasing trend, suggesting a growing rainfall trend in the trimmed input data. It is evident that the positive portion of the relative bias curve constitutes the majority, that is, for $\mathbf{x}_L(t_0)$, the declining and oscillating parts of the trimmed input data dominate, whereas the growing trend occupies only a small portion. We consider this as the main reason for the misjudgment of rainfall trends by the CT-DMD model.

Fig. 27 shows the DMD eigenvalues extracted from the processed input data; it can be observed that the magnitudes of the DMD eigenvalues are all less than 1, and the DMD eigenvalues have nonzero imaginary components. This indicates that the CT-DMD model interprets the processed input data as declining data with an oscillatory behavior. This is consistent with our analysis.

C. Summary of Case Study

From the analysis of the 33rd and 22nd subsets, the following conclusions can be drawn.

1) *22nd Subset:* For initial state vector $\mathbf{x}_L(t_0)$, when only a single trend (growing or declining) is present in the input data and this trend is consistent with the trend in the forecast data, the CT-DMD model can forecast the data accurately.
2) *33rd Subset:* For initial state vector $\mathbf{x}_L(t_0)$, when both growing and declining trends are present in the input data, it may impact the CT-DMD model's ability to accurately judge the rainfall trend in the forecast data.

Therefore, the capability of the CT-DMD model to analyze data with complex variations in rainfall trends requires further enhancement.

According to the forecasting principles of the CT-DMD, we have reason to believe that the CT-DMD model's superiority in rainfall forecasting is not limited to the rainfall data presented in this article. As seen in (6), the forecasting mechanism of the CT-DMD for rainfall intensity variation involves DMD modes Φ, DMD eigenvalues Λ, and initial vector $\mathbf{x}_L(t_0)$. Through analyzing DMD modes Φ, DMD eigenvalues Λ, and initial vector $\mathbf{x}_L(t_0)$, we can capture and forecast variations in rainfall intensity, including growing, declining, and oscillation, which can fully represent the characteristics of rainfall intensity variation. The CT-DMD model's forecasting of atmospheric motion relies on the optical flow model, which has been extensively utilized in the field of rainfall nowcasting [14], [34], [35], and its effectiveness has been validated [7]. Therefore, although the capability of the CT-DMD model to analyze data with complex variations in rainfall trends requires further enhancement, given its better performance on most subset data compared to the Rainymotion model, we have reason to believe that the CT-DMD model holds potential for application to rainfall data beyond the scope of this article.

VI. Conclusion

Lagrangian persistence method in nowcasting, employed for short-term weather forecasting, is a method of forecasting future weather conditions by extrapolating recent weather conditions. However, the difficulty in analyzing the intensity variation of meteorological physical quantities deteriorates its performance toward long-term forecasting or in situations of rapid weather changes.

In this study, we integrated the optical flow model with the DMD model, providing an effective solution for analyzing the intensity variation of meteorological physical quantities in the Lagrangian persistence method. The proposed CT-DMD model was evaluated using radar-observed rainfall data from the Kanto region of Japan, and the Rainymotion model was used as a benchmark. When the lead time was 5 min, 22.22% of the subsets in the experimental dataset showed that the CT-DMD model had a higher forecast accuracy than the Rainymotion model. When the lead time was 15 min, 68.89% of the subsets in the experimental dataset showed that the CT-DMD model had a higher forecast accuracy than the Rainymotion model. When the lead time was 25 min, 88.89% of the subsets in the experimental dataset showed that the CT-DMD model had a higher forecast accuracy than the Rainymotion model. The accuracy advantage of the CT-DMD model became apparent after a lead time of 15 min and became increasingly significant as the lead time increased.

From the understanding of the principles of the model and the discussion of the case study, it can be observed that the analysis of rainfall intensity variation by the CT-DMD model depends on the trend of rainfall intensity variation in the input data. When only a single trend (growing or declining) was present in the input data and this trend was consistent with that in the forecast data, the CT-DMD model could forecast the data accurately; however, when both growing and declining trends were present in the input data, the ability of the CT-DMD model to accurately judge the rainfall trend in the forecast data was impacted. In future research, we aim to address this shortcoming by adding additional meteorological variables and considering their effective combination.

For future research directions, we currently have two specific areas of focus. The first one involves enhancing the analysis and predictive capabilities of the CT-DMD model for input data with complex variations in rainfall trends. The second one is to expand the dataset, testing the CT-DMD model's predictive performance across various types and scales of rainfall, and comparing it with the corresponding forecasting models.

References

[1] B. W. Golding, "Nimrod: A system for generating automated very short range forecasts," *Meteorolog. Appl.*, vol. 5, no. 1, pp. 1–16, Mar. 1998.
[2] C. Pierce, A. Seed, S. Ballard, D. Simonin, and Z. Li, "Nowcasting," in *Doppler Radar Observations: Weather Radar, Wind Profiler, Ionospheric Radar, and Other Advanced Applications*, J. Bech and J. L. Chau, Eds. Rijeka, Croatia: IntechOpen, 2012, pp. 97–142.
[3] J. Sun, "Convective-scale assimilation of radar data: Progress and challenges," *Quart. J. Roy. Meteorological Soc.*, vol. 131, no. 613, pp. 3439–3463, Oct. 2005.
[4] M. Buehner and D. Jacques, "Non-Gaussian deterministic assimilation of radar-derived precipitation accumulations," *Monthly Weather Rev.*, vol. 148, no. 2, pp. 783–808, Feb. 2020.
[5] K. A. Browning, "Review lecture: Local weather forecasting," *Proc. Roy. Soc. London, A. Math. Phys. Sci.*, vol. 371, no. 1745, pp. 179–211, 1745.
[6] G. Austin and A. Bellon, "The use of digital weather radar records for short-term precipitation forecasting," *Quart. J. Roy. Meteorolog. Soc.*, vol. 100, no. 426, pp. 658–664, Oct. 1974.

[7] A. Georgy, H. Maik, and T. Winterrath, "Optical flow models as an open benchmark for radar-based precipitation nowcasting (rainymotion v0. 1)," *Geosci. Model Develop.*, vol. 12, no. 4, pp. 1387–1402, 2019.

[8] C. Mueller et al., "NCAR auto-nowcast system," *Weather Forecasting*, vol. 18, no. 4, pp. 545–561, 2003.

[9] U. Germann and I. Zawadzki, "Scale-dependence of the predictability of precipitation from continental radar images. Part I: Description of the methodology," *Monthly Weather Rev.*, vol. 130, no. 12, pp. 2859–2873, Dec. 2002.

[10] T. Winterrath, W. Rosenow, and E. Weigl, "On the DWD quantitative precipitation analysis and nowcasting system for real-time application in German flood risk management," *IAHS-AISH Publication*, vol. 10, no. 351, pp. 323–329, 2012.

[11] N. E. Bowler, C. E. Pierce, and A. W. Seed, "STEPS: A probabilistic precipitation forecasting scheme which merges an extrapolation nowcast with downscaled NWP," *Quart. J. Roy. Meteorolog. Soc.*, vol. 132, no. 620, pp. 2127–2155, Oct. 2006.

[12] L. Foresti, M. Reyniers, A. Seed, and L. Delobbe, "Development and verification of a real-time stochastic precipitation nowcasting system for urban hydrology in Belgium," *Hydrol. Earth Syst. Sci.*, vol. 20, no. 1, pp. 505–527, Jan. 2016.

[13] P. Cheung and H. Yeung, "Application of optical-flow technique to significant convection nowcast for terminal areas in Hong Kong," in *Proc. 3rd WMO Int. Symp. Nowcasting Very Short-Range Forecasting*, 2012, pp. 6–10.

[14] W.-C. Woo and W.-K. Wong, "Operational application of optical flow techniques to radar-based rainfall nowcasting," *Atmosphere*, vol. 8, no. 3, p. 48, Feb. 2017.

[15] S. Xingjian, C. Zhourong, W. Hao, Y. Dit-Yan, W. Wai-Kin, and W. Wang-Chun, "Convolutional LSTM network: A machine learning approach for precipitation nowcasting," in *Proc. 28th Int. Conf. Neural Inf. Process. Syst. (NIPS)*, vol. 1, 2015, pp. 802–810.

[16] X. Shi et al., "Deep learning for precipitation nowcasting: A benchmark and a new model," in *Proc. Adv. Neural Inf. Process. Syst.*, 2017, pp. 5617–5627.

[17] S. P. Van, H. M. Le, D. V. Thanh, T. D. Dang, H. H. Loc, and D. T. Anh, "Deep learning convolutional neural network in rainfall–runoff modelling," *J. Hydroinformatics*, vol. 22, no. 3, pp. 541–561, May 2020.

[18] D. Sun, J. Wu, H. Huang, R. Wang, F. Liang, and H. Xinhua, "Prediction of short-time rainfall based on deep learning," *Math. Problems Eng.*, vol. 2021, pp. 1–8, Mar. 2021.

[19] O. Sharma, D. Trivedi, S. Pattnaik, V. Hazra, and N. B. Puhan, "Improvement in district scale heavy rainfall prediction over complex terrain of North East India using deep learning," *IEEE Trans. Geosci. Remote Sens.*, vol. 61, 2023, Art. no. 4106408.

[20] J. Byun, C. Jun, J. Kim, J. Cha, and R. Narimani, "Deep learning-based rainfall prediction using cloud image analysis," *IEEE Trans. Geosci. Remote Sens.*, vol. 61, 2023, Art. no. 4701411.

[21] R. Wang, L. Su, W. K. Wong, A. K. H. Lau, and J. C. H. Fung, "Skillful radar-based heavy rainfall nowcasting using task-segmented generative adversarial network," *IEEE Trans. Geosci. Remote Sens.*, vol. 61, 2023, Art. no. 4103613.

[22] G. Ayzel, T. Scheffer, and M. Heistermann, "RainNet v1.0: A convolutional neural network for radar-based precipitation nowcasting," *Geosci. Model Develop.*, vol. 13, no. 6, pp. 2631–2644, Jun. 2020.

[23] S. L. Brunton, J. L. Proctor, J. N. Kutz, and W. Bialek, "Discovering governing equations from data by sparse identification of nonlinear dynamical systems," *Proc. Nat. Acad. Sci. USA*, vol. 113, no. 15, pp. 3932–3937, 2016.

[24] S. H. Rudy, S. L. Brunton, J. L. Proctor, and J. N. Kutz, "Data-driven discovery of partial differential equations," *Sci. Adv.*, vol. 3, no. 4, pp. 3932–3937, Apr. 2017.

[25] M. Raissi, P. Perdikaris, and G. E. Karniadakis, "Machine learning of linear differential equations using Gaussian processes," *J. Comput. Phys.*, vol. 348, pp. 683–693, Nov. 2017.

[26] M. Raissi, P. Perdikaris, and G. E. Karniadakis, "Numerical Gaussian processes for time-dependent and nonlinear partial differential equations," *SIAM J. Sci. Comput.*, vol. 40, no. 1, pp. A172–A198, Jan. 2018.

[27] H. R. Pruppacher and J. D. Klett, *Microphysics of Clouds and Precipitation*. Dordrecht, The Netherlands: Springer, 1996.

[28] R. Kato, K.-I. Shimose, and S. Shimizu, "Predictability of precipitation caused by linear precipitation systems during the July 2017 northern Kyushu heavy rainfall event using a cloud-resolving numerical weather prediction model," *J. Disaster Res.*, vol. 13, no. 5, pp. 846–859, Oct. 2018.

[29] J. R. Holton and G. J. Hakim, *An Introduction to Dynamic Meteorology*. Amsterdam, The Netherlands: Academic, 2012.

[30] B. K. P. Horn and B. G. Schunck, "Determining optical flow," *Artif. Intell.*, vol. 17, nos. 1–3, pp. 185–203, Aug. 1981.

[31] J. J. Gibson, *The Perception of the Visual World*. Boston, MA, USA: Houghton Mifflin, 1950.

[32] J. J. Gibson, *The Senses Considered As Perceptual Systems*. Boston, MA, USA: Houghton Mifflin, 1966.

[33] J. J. Gibson, "On the analysis of change in the optic array," *Scandin. J. Psychol.*, vol. 18, no. 1, pp. 161–163, Sep. 1977.

[34] N. E. H. Bowler, C. E. Pierce, and A. Seed, "Development of a precipitation nowcasting algorithm based upon optical flow techniques," *J. Hydrol.*, vol. 288, nos. 1–2, pp. 74–91, Mar. 2004.

[35] Y. Liu, D.-G. Xi, Z.-L. Li, and Y. Hong, "A new methodology for pixel-quantitative precipitation nowcasting using a pyramid Lucas Kanade optical flow approach," *J. Hydrol.*, vol. 529, pp. 354–364, Oct. 2015.

[36] T. Kroeger, R. Timofte, D. Dai, and L. Van Gool, "Fast optical flow using dense inverse search," in *Proc. Eur. Conf. Comput. Vis.* Cham, Switzerland: Springer, 2016, pp. 471–488.

[37] P. J. Schmid, "Dynamic mode decomposition of numerical and experimental data," *J. Fluid Mech.*, vol. 656, pp. 5–28, Jul. 2010.

[38] S. L. Brunton and J. N. Kutz, *Data-Driven Science and Engineering: Machine Learning, Dynamical Systems, and Control*. Cambridge, U.K.: Cambridge Univ. Press, 2020.

[39] Z. Huang, T. Li, K. Huang, H. Ke, M. Lin, and Q. Wang, "Predictions of flow and temperature fields in a T-junction based on dynamic mode decomposition and deep learning," *Energy*, vol. 261, Dec. 2022, Art. no. 125228.

[40] Y. Yu, Y. Zhang, S. Qian, S. Wang, Y. Hu, and B. Yin, "A low rank dynamic mode decomposition model for short-term traffic flow prediction," *IEEE Trans. Intell. Transp. Syst.*, vol. 22, no. 10, pp. 6547–6560, Oct. 2021.

[41] Y. Shang, "Matrix-scaled consensus on weighted networks with state constraints," *IEEE Syst. J.*, vol. 17, no. 4, pp. 6472–6479, Jun. 2023.

[42] J. H. Tu, C. W. Rowley, D. M. Luchtenburg, S. L. Brunton, and J. N. Kutz, "On dynamic mode decomposition: Theory and applications," *J. Comput. Dyn.*, vol. 1, no. 2, pp. 391–421, 2014.

[43] N. Demo, M. Tezzele, and G. Rozza, "PyDMD: Python dynamic mode decomposition," *J. Open Source Softw.*, vol. 3, no. 22, p. 530, Feb. 2018.

[44] J. Sesterhenn and A. Shahirpour, "A characteristic dynamic mode decomposition," *Theor. Comput. Fluid Dyn.*, vol. 33, nos. 3–4, pp. 281–305, Aug. 2019.

[45] G. K. Batchelor, *An Introduction To Fluid Dynamics*. Cambridge, U.K.: Cambridge Univ. Press, 1967.

[46] M. Maki et al., "Semi-operational rainfall observations with X-band multi-parameter radar," *Atmos. Sci. Lett.*, vol. 6, no. 1, pp. 12–18, Jan. 2005.

[47] Y. Shang, "Subgraph robustness of complex networks under attacks," *IEEE Trans. Syst. Man, Cybern., Syst.*, vol. 49, no. 4, pp. 821–832, Apr. 2019.

[48] A. H. Murphy, "Skill scores based on the mean square error and their relationships to the correlation coefficient," *Monthly Weather Rev.*, vol. 116, no. 12, pp. 2417–2424, Dec. 1988.

[49] J. E. Nash and J. V. Sutcliffe, "River flow forecasting through conceptual models Part I—A discussion of principles," *J. Hydrol.*, vol. 10, no. 3, pp. 282–290, Apr. 1970.

[50] Z. Huang and T. Zhao, "Predictive performance of ensemble hydroclimatic forecasts: Verification metrics, diagnostic plots and forecast attributes," *WIREs Water*, vol. 9, no. 2, p. e1580, Mar. 2022.

Shitao Zheng received the Ph.D. degree from the University of Yamanashi, Kofu, Japan, in 2023.

He is currently a Project Researcher at The University of Tokyo, Bunkyo, Japan. His research interests include data-driven models and their applications.

Takashi Miyamoto (Member, IEEE) received the B.S., M.S., and Ph.D. degrees in civil engineering from The University of Tokyo, Bunkyo, Japan, in 2007, 2009, and 2012, respectively.

He is currently an Associate Professor at the University of Yamanashi, Kofu, Japan. He is also a Visiting Scholar at German Research Center for Artificial Intelligence, Kaiserslautern, Germany. His research interests include data-driven science, disaster mitigation engineering, and applied mechanics.

Shingo Shimizu received the B.S. degree in Earth sciences from Hokkaido University, Sapporo, Japan, in 2001, and the M.S. and Ph.D. degrees from Nagoya University, Nagoya, Japan, in 2003 and 2007, respectively.

He is currently a Senior Researcher at the National Research Institute for Earth Science and Disaster Resilience, Tsukuba, Japan. His field of study is data assimilation using mesoscale meteorological forecasts and radar analysis.

Ryohei Kato received the B.S., M.S., and Ph.D. degrees in Earth sciences from Kyushu University, Fukuoka, Japan in 2006, 2008, and 2012, respectively.

He is currently the Chief Researcher at the National Research Institute for Earth Science and Disaster Resilience, Tsukuba, Japan. He specializes in very short-range forecasting of severe local storms using a combination of nowcasting, numerical weather prediction (NWP) models with data assimilation, and blending techniques.

Koyuru Iwanami received the B.S., M.S., and D.S. degrees in geophysics from Hokkaido University, Sapporo, Japan, in 1985, 1987, and 1991, respectively.

He is currently the Vice President (Research) at the National Research Institute for Earth Science and Disaster Resilience, Tsukuba, Japan. His research interests include radar meteorology.